Spin-phonon coupling and high-pressure phase transitions of RMnO_{3} (R=Ca and Pr): An inelastic neutron scattering and first-principles study

S. K. Mishra, M. K. Gupta, R. Mittal, A. I. Kolesnikov, and S. L. Chaplot

Phys. Rev. B **93**, 214306 — Published 22 June 2016

DOI: 10.1103/PhysRevB.93.214306

Spin-Phonon Coupling and High Pressure Phase Transitions of $RMnO_3$ (R= Ca and Pr): An Inelastic Neutron Scattering and First Principle Studies

S. K. Mishra[1], M. K. Gupta[1], R. Mittal[1], A. I. Kolesnikov[2] and S. L. Chaplot[1]
[1]*Solid State Physics Division, Bhabha Atomic Research Centre, Mumbai 400085, India*
[2]*Chemical and Engineering Materials Division, Oak Ridge National Laboratory, Oak Ridge, Tennessee 37831, USA*

We report inelastic neutron scattering measurements over 7-1251 K in $CaMnO_3$ covering various phase transitions, and over 6-150 K in $PrMnO_3$ covering the magnetic transition. The excitations around 20 meV in $CaMnO_3$ and at 17 meV in $PrMnO_3$ at low temperatures are found to be associated with magnetic origin. We observe coherent magnetic neutron scattering in localized regions in reciprocal-space and show it to arise from long-range correlated magnetic spin-waves below the magnetic transition temperature (T_N) and short-range stochastic spin-spin fluctuations above T_N. In spite of similarity of the structure of the two compounds, the neutron inelastic spectrum of $PrMnO_3$ exhibits broad features at 150 K unlike well-defined peaks in the spectrum of $CaMnO_3$. This might result from the difference in nature of interactions in the two compounds (magnetic and Jahn-Teller distortion). Ab-initio phonon calculations have been used to interpret the observed phonon spectra. The ab-initio calculations at high pressures show that the variations of Mn-O distances are isotropic for $CaMnO_3$ and highly anisotropic for $PrMnO_3$. The calculation in $PrMnO_3$ shows the suppression of Jahn-Teller distortion and simultaneous insulator to metal transition. It appears that this transition may not be associated with the occurrence of the tetragonal phase above 20 GPa as reported in the literature, since the tetragonal phase is found to be dynamically unstable although it is found to be energetically favored over the orthorhombic phase above 20 GPa. $CaMnO_3$ does not show any phase transition up to 60 GPa.

PACS numbers: 78.70.Nx, 63.20.-e, 61.50.Ks, 65.40.-b

Keywords: Neutron inelastic scattering, Spin waves, Phonons in crystal lattice, Crystallographic aspects of phase transformations; pressure effects, Thermal properties of crystalline solids

I. INTRODUCTION

The perovskite transition-metal oxides show a variety of interesting physical properties, such as dielectric, magnetic, optical, and transport properties [1-10]. The study of perovskite manganite $RMnO_3$ (R= Ca, La, Pr etc) has been of great relevance [6-17]. Among these, $CaMnO_3$ has received much interest in the past decade due to its structural [18], physical [19], magnetic [20], and thermo-electrical properties [21,22].

$CaMnO_3$ crystallizes in the distorted orthorhombic structure (space group Pnma) and consists of single-valent Mn^{4+} ions and does not exhibit Jahn-Teller distortion. At ambient conditions, it is paramagnetic and at ~130 K it undergoes a G type antiferromagnetic (AFM) transition [23]. In high temperature x-ray diffraction study, Taguchi *et al* [24] showed that oxygen deficient $CaMnO_3$ undergoes orthorhombic to tetragonal phase (*I4/mcm*) transition at 1169 K and finally transforms to cubic phase (*Pm-3m*) at 1186 K. Doping of trivalent and tetravalent ions at Ca^{2+} site provides additional electrons into e_g orbital of Mn ions and causes a variety of phase transitions, e.g from collinear G-type AFM insulator to canted G-type AFM metal, collinear C-type AFM insulator etc. This suggests that we can tune the magnetic phase transition with a small amount of electron doping. For example, solid solution of (1-x)$CaMnO_3$- x$PrMnO_3$ ($Ca_{1-x}Pr_xMnO_3$) exhibits a variety of ground state, namely: G-AFM insulator, CE- type charge ordered state, CE-type AFM spins ordering, canted AFM state which consists a mixture of AFM and ferromagnetic (FM) clusters, depending on temperature and composition [25-28]. The other end member of solid solution, $PrMnO_3$ also crystallizes in the orthorhombic phase but it exhibits [16] a strong Jahn-Teller distortion of MnO_6 octahedra associated with the ordering of e_g orbital and undergoes A-type antiferromagnetic spin ordering below 95 K [16]. The difference between the magnetic structures of $CaMnO_3$ and $PrMnO_3$ is attributed to different occupancy of d electron in Mn ions. Hence it is intriguing to study the role of magnetic interaction on lattice vibration.

The structural, physical and magnetic properties of $RMnO_3$ (R= Ca and Pr) were investigated by variety of experimental techniques [29-36]. The physical properties of these materials are governed by a delicate interplay of charge, spin, orbital, and lattice degrees of freedom. To understand the relation among these interactions, first principles calculations have been performed in cubic and orthorhombic phases. Using a density functional theory approach within the local spin density approximation, Bhattacharjee *et al*, [33] computed structural, dielectric and dynamical properties of orthorhombic phase of $CaMnO_3$. They computed the zone-center phonon modes and proposed assignment of experimental data. Zhang *et al* [34] investigated geometry, ground state electronic structure and charge distributions of $CaMnO_3$. Effect of compressive and tensile strains on a magnetic phase transition in electron-doped $CaMnO_3$ was theoretically studied by Tsukahara *et al* [35]. Further the first principles calculations of

structural, electronic and magnetic properties of the $PrMnO_3$ as well as the calculation of zone centre phonon modes in the cubic phase were reported by Bouadjemi [36].

The spin dynamical properties and energy of the exchange interactions in magnetic materials are mostly determined by using inelastic neutron scattering on single crystal samples. A variety of magnetic materials likes (La, Ca) MnO_3, $TmFeO_3$, $ErFeO_3$, $YFeO_3$ [37] have been characterized and exchange interactions were identified. McQueeney *et al* [38] have shown that the different exchange interactions and spin waves spectrum in ABO_3 perovskite materials can also be evaluated using inelastic neutron scattering on powder samples.

Understanding of various functional properties of derived compounds $Pr_xCa_{1-x}MnO_3$ needs complete study of magnetic and dynamical properties of the parent compounds $CaMnO_3$ and $PrMnO_3$. In the present study, we report results of inelastic neutron scattering measurements at different temperatures of $CaMnO_3$ and $PrMnO_3$. We have identified coherent magnetic neutron scattering in localized regions in reciprocal-space that arises from long-range correlated magnetic spin-waves below T_N and short-range stochastic spin-spin fluctuations above the magnetic transition temperature (T_N). We have also extracted the temperature dependence of phonon spectra for $CaMnO_3$ and $PrMnO_3$. The interpretation and analysis of the observed phonon spectra have been performed using ab-initio phonon calculations. We have extended the ab-initio calculations of the ground-state orthorhombic phase in the entire Brillouin zone. Differences in the nature of interactions between the two compounds lead to noticeable differences in the nature of the phonon spectra. Section II and III describe the experimental and theoretical methods employed. The results of the temperature dependent neutron experiments in the two compounds and its interpretation in terms of the magnetic and phonon excitations are discussed in Sec. IV (a-d).

Recently, Mota *et al.* [13] reported a high pressure study in which they observed changes in the x-ray diffraction patterns of $PrMnO_3$ and disappearance of the Raman spectrum at 45 GPa. The authors [13] suspected that the changes might be related to the structural phase transition from orthorhombic to tetragonal structure. However, the disappearance of Raman peaks could also be due to insulator to metal transition. With a view to overcome this ambiguity we have performed the first-principles calculations to investigate the effect of pressure on the structural distortions in the orthorhombic phase. The results are discussed in Sec. IV(e). The calculated structure as a function of pressure in $PrMnO_3$ shows that suppression of Jahn-Teller distortion and insulator to metal transition occurs simultaneously. We find that the tetragonal phase is energetically favored over the orthorhombic phase above 20 GPa, but is dynamically unstable. Some additional results on unstable phonon modes in the cubic (*Pm-3m*) phase that lead to stabilization of the tetragonal phase at high temperature are discussed in Appendix.

II. EXPERIMENT

Polycrystalline samples of $CaMnO_3$ and $PrMnO_3$ were prepared by a solid state reaction method using powders of $CaCO_3$, Pr_6O_{11} and MnO_2 each of minimum 99.5% purity. These powders were thoroughly mixed in stoichiometric amounts using zirconia jar and balls in a ball mill using acetone as the mixing medium. Calcination of the mixed powder was carried out at different temperatures and duration with several intermediate grindings. The calcined powder was characterized using x-ray diffraction and the temperature and duration were optimized for single phase purity. Single phase calcined powder was pressed into circular pellets of 12 mm diameter and ~1.25 mm thickness using a uniaxial hydraulic press at an optimized load of 100 kN. Sintering of the green pellets was carried out at 1700 K for 20 hours in air. For powder x-ray diffraction experiments, the sintered pellets were crushed to fine powder and subsequently annealed at 750 K to remove any strains introduced during crushing. The phase purity of the samples was confirmed by x-ray powder diffraction recorded using Cu K_α radiation in the angular range 20 -130 degrees at room temperature.

Inelastic neutron scattering measurements were performed using the Fine Resolution Chopper Spectrometer (SEQUOIA) [39,40] at the Spallation Neutron Source (SNS) at Oak Ridge National Laboratory. The data were collected using fixed incident neutron energy of 110 meV, which allowed for the measurement of excitations up to energy transfers of ~100 meV. The low temperatures scans (4-300 K) were carried out using the closed cycle helium refrigerator. For high temperature measurements up to 1250 K samples were heated in air. The low temperature (T<305 K) measurements of $CaMnO_3$ were done with high energy resolution, providing resolution of ΔE=2.0 meV at the elastic line. All other measurements were done in high intensity configuration, with energy resolution of ΔE=5.5 meV at elastic line. The resolution in both settings becomes better with increasing energy transfer and around 80 meV it reaches about 1/3 of that at the elastic line. We have used a furnace (called MiCAS) with a quartz tube insert that allows controlling the atmosphere of sample.

In the incoherent one-phonon approximation, the phonon part of the scattering function $S(Q,E)$, as observed in the neutron experiments, is related to the neutron-weighted phonon density of states [41] as follows:

$$g^{(n)}(E) = A < \frac{e^{2W(Q)}}{Q^2} \frac{E}{n(E,T) + \frac{1}{2} \pm \frac{1}{2}} S(Q,E) > \qquad (1)$$

$$g^{n}(E) = B\sum_{k}\{\frac{4\pi b_{k}^{2}}{m_{k}}\}g_{k}(E) \qquad (2)$$

where Q and E are neutron momentum and energy transfers, respectively, the + or – signs correspond to energy loss or gain of the neutrons respectively and $n(E,T) = [\exp(E/k_{B}T) - 1]^{-1}$. A and B are normalization constants and b_k , m_k , and $g_k(E)$ are, respectively, the neutron scattering length, mass, and partial density of phonon states of the k^{th} atom in the unit cell. The quantity within < ---- > represents suitable average over all Q values at a given energy. $2W(Q)$ is the Debye-Waller factor averaged over all the atoms. The weighting factors $4\pi b_{k}^{2}/m_{k}$ for various atoms in the units of barns/amu are: Ca: 0.071; Pr: 0.019; Mn: 0.039; O: 0.264. The MANTIDPLOT [42] and DAVE [43] software packages were used for data reduction and analysis. The data were collected over a wide range of Q up to 7 $Å^{-1}$. Since both the compounds contain magnetic atoms, contributions from magnetic scattering are also present in the measured data.

III. THEORETICAL CALCULATIONS

The calculation of phonon spectra has been performed using the first-principles density functional theory in both the local density approximation (LDA) and generalized gradient approximation (GGA) for $CaMnO_3$. However, for $PrMnO_3$, only GGA has been used. Relaxed geometries and total energies were obtained using the projector-augmented wave formalism [44, 45] of the Kohn-Sham formulation of the density-functional theory [46, 47] within both the LDA and GGA as implemented in the Vienna *ab initio* simulation package (VASP) [48]. The GGA was formulated by the Perdew-Burke-Ernzerhof (PBE) density functional [49] and LDA was based on the Ceperly–Alder parametrization by Perdew and Zunger [50]. All results are well converged with respect to k mesh and energy cutoff for the plane-wave expansion. The total energy calculations have been done using an energy cutoff of 1100 eV. A grid of 8×8×8 K-points was used according to the Monkhorst-Pack (MP) scheme [51]. The convergence criteria for the self-consistent field and for the ionic relaxation loops were set to 10^{-8} eV $Å^{-1}$ and 10^{-4} eV $Å^{-1}$, respectively. Hellmann-Feynman forces following geometry optimization were less than 10^{-4} eV $Å^{-1}$.

We have used the G-type and A-type antiferromagnetic structures in orthorhombic phases for $CaMnO_3$ and $PrMnO_3$ respectively. The choice of magnetic structures is based on the previously reported configurations obtained from neutron diffraction measurements [16, 23]. However, in the

tetragonal phase of $PrMnO_3$, the magnetic structure is not known. So we have calculated the enthalpy of the tetragonal phase of $PrMnO_3$ including different antiferromagnetic configurations, namely A, C and G type, and ferromagnetic configurations. The calculations show that ferromagnetic structure is favored in comparison to the other structures. In the cubic phase, G-type antiferromagnetic and ferromagnetic structures are adapted for $CaMnO_3$ and $PrMnO_3$ respectively.

The supercell approach or direct method is used to calculate the phonon frequencies in entire Brillouin zone implemented in PHONON5.12 software [52]. The supercell of dimension 2×2×2 has been used to calculate the Hellman-Feynman forces in the orthorhombic and the tetragonal phases. For the calculation in the high temperature cubic phase, which has a small unit cell containing 5 atoms, we have chosen a supercell of dimension 4×4×4 to properly account the long range interaction. The forces are extracted from individual displacements of the symmetry inequivalent atoms in the super cell along three Cartesian directions ((±x, ±y, ±z). In the orthorhombic phase, 24 distinct configurations are generated by displacing the symmetrically inequivalent atoms. However, in tetragonal and cubic phases, 16 and 8 distinct displacements are found respectively.

The phonon calculations are performed in various magnetic and nonmagnetic configurations to see the effect of spin degrees of freedom on phonons. The experimental structure and the measured neutron inelastic spectrum are found to be better described by the calculations when the magnetic degrees of freedom are included, reflecting that the lattice couples to the magnetic structure. These calculations enable us to quantify the strength of the coupling between spin and phonons. Hereafter, the labeling "FRM" and "FRNM" refer to fully relaxed magnetic and fully relaxed nonmagnetic calculation. The nonmagnetic calculations are done in fully relaxed and partially relaxed geometry. In the fully relaxed nonmagnetic calculations, the atomic coordinates and lattice parameter have been relaxed. However, partially relaxed nonmagnetic calculation (PNM) refers to only relaxing the atomic coordinates and keeping the lattice parameter fixed as used in magnetic calculations.

IV. RESULTS AND DISCUSSION

We first present the neutron inelastic spectra and its temperature dependence in $CaMnO_3$ and $PrMnO_3$ in section (a) and (b) respectively. We also discuss below the interpretation in terms of magnetic and phonon contribution to the neutron spectra. In section (c) we extract information on the spin wave density of states. Section (d) deals with the first principle DFT calculation of the phonon spectra taking into account the magnetic structure. Then in section (e) we apply the same ab-initio calculation to understand certain ambiguity of structural and insulator to metal transitions at high pressure as reported in the literature [13].

(a) Temperature dependence of neutron inelastic spectra in orthorhombic phase of $CaMnO_3$

$CaMnO_3$ is known to undergo paramagnetic to antiferromagnetic (AFM) transition at $T_N \sim 130$ K [23]. Other transitions are observed from orthorhombic to tetragonal phase at 1169 K and then to cubic phase at 1186 K. The neutron inelastic spectra of $CaMnO_3$ (Figs. 1-3) were measured from 7 K to 1250 K, across the magnetic transition (~130 K) and the structural phase transitions at high temperatures**.** The data were collected over wide range of momentum transfer (Q) from 0.5-7 $Å^{-1}$. The magnetic signal is expected to be more pronounced at low Q, and it decreases as Q increases, following the magnetic form factor. In contrast to this, in the case of phonons, the intensity increases with Q in the low-Q region showing a Q^2 like dependence. Hence we have integrated the inelastic scattering function S(Q,E) in two ranges, namely total Q range (0.5-7 $Å^{-1}$) and high Q (4-7 $Å^{-1}$), the latter one represents mostly the contribution from the neutron scattering on phonons.

The data collected at 7 K show an intense peak at about 20 meV in the low Q data (Figs. 1, 2). This peak is largely contributed from magnetic excitations as it shows strong Q dependence of intensity (stronger at low-Q and weaker at high-Q). Moreover as the temperature increases, the contribution from spin excitation is expected to become weaker. Above the magnetic transition temperature (T_N=130 K) we also see that the intensity of peak at 20 meV is decreasing with increase in temperature up to 601 K (Fig. 4). This indicates that the contributions from the paramagnetic scattering persist up to very high temperatures of 601 K. At temperatures of 951 K and above, the intensity does not change with increase in temperature, which reflects residual phonon contribution.

Figure 2 illustrates the experimental S(Q,E) in the low temperature range from 7 to 300 K. The data collected at 7 K clearly show the signature of spin-wave excitations, which are probably gaped at Q=1.45 $Å^{-1}$, corresponding to magnetic Bragg peak (011) (the gap is not resolved with the current experimental setup, providing energy resolution ~2 meV at the elastic line). Further we notice that at higher temperature (T=110 K), the intensity of these excitations are strongly redistributed to lower energies, and in particular, the peak position shifts from 19.5 meV at 7 K to 16.5 meV at 110 K. At $T>T_N$ (in paramagnetic state) at small Q values (Q<3.5 $Å^{-1}$), we observe spin-fluctuation excitations that extend from the elastic line up to ~20 meV. The inelastic neutron scattering spectrum at T=110 K (just below T_N, Fig. 3) shows that clear spin-wave excitations propagate with increasing intensity to higher energies starting at low energies and Q=1.47 $Å^{-1}$. At T=140 K ($T>T_N$), there is no long range magnetic order in the sample and the elastic magnetic peak at Q=1.47 $Å^{-1}$ disappears (see Fig. 3). The inelastic neutron scattering spectrum around this Q area shows much broader features. While at higher Q (Q=1.2 to 1.5 $Å^{-1}$) they look like quasi-elastic neutron scattering (QENS) signal, at smaller Q (Q=0.9 to 1.2 $Å^{-1}$) they look like over-damped dispersed excitations. We notice that the excitations are localized around

Q=0.8-1.6 $Å^{-1}$; therefore, the scattering should be coherent. In the case of incoherent scattering, the signal will be almost Q-independent. At higher temperature (300 K) the spectral features in this range look more like typical quasielastic signal, but they are still localized in Q-space, so this spectrum relate to coherent neutron scattering from strongly disordered spin-spin fluctuations. It appears that the nature of neutron scattering intensity S(Q,E) changes above T_N from long-range correlated magnetic spin-waves to short-range stochastic spin-spin fluctuations, and the intensity being still localized in Q- space, spreads over a broader range of Q. The intensity of these spin fluctuations corrected for the thermal population Bose factor leads to a peak in $g^{(n)}(E)$, which is plotted in Figs. 1 & 3, that decreases with temperature increase.

The excitation around 17-18 meV at Q=6 $Å^{-1}$ (in Fig. 2) increases its intensity with temperature (at $T>T_N$). The intensity of the magnetic excitations should strongly decrease, so this excitation should be due to phonons. However, at lower Q (~4.5 $Å^{-1}$) the intensity at 17 meV dropped too abruptly, that may be due to strongly dispersed phonon modes. So, in this case we cannot expect the intensity of this excitation at lower Q range to vary Q^2.

The high temperature neutron inelastic spectra (Fig. 4) show strong modification with increasing temperature. In particular, with increasing temperature up to 601 K, the intensity of peaks below 40 meV decreases while the peak around 90 meV shows significant shift towards lower energies. The others peaks do not change in a noticeable way. We find that above 601 K, a prominent change is observed in the neutron inelastic spectra, where they are found to be more diffusive as compared to the spectra at low temperatures. These changes in the phonon spectra may be associated with phase transitions in $CaMnO_3$ which transforms from the orthorhombic to the tetragonal phase at 1169 K, and finally to cubic phase at 1186 K [24].

(b) Temperature dependent neutron inelastic spectra in orthorhombic phase of $PrMnO_3$

The compound $PrMnO_3$ is isostructural to $CaMnO_3$; however, the magnetic structure is different. The Jahn-Teller transition in $PrMnO_3$ takes place at about 1050 K. It undergoes antiferromagnetic spin ordering below 95 K. Here we measured the neutron inelastic spectra of $PrMnO_3$ at two temperatures, 6 and 150 K. The experimental S(Q,E) data (Fig. 5, at the bottom) collected at 6 K clearly show the signature of spin-wave excitations at energies below 20 meV and Q<1.5 $Å^{-1}$, which significantly dissipate at 150 K. Figure 5 (at the top) shows the neutron inelastic spectra, (a) summed over momentum transfer (Q) =1-7 $Å^{-1}$ and (b) Q=4-7 $Å^{-1}$. The data collected at 6 K show intense excitations with the peak maximum at about 17 meV. However, above the magnetic transition

temperature, the intensity at 17 meV peak is significantly suppressed but has contribution from phonons and paramagnetic fluctuations.

It is remarkable to notice that in spite of similar structure, the room temperature neutron inelastic spectrum (Fig. 1) of $CaMnO_3$ exhibits well-defined peaks in comparison to the data for $PrMnO_3$ (Fig. 5) at 150 K. The differences in the phonon spectra may be due to the difference in nature of interatomic interactions. The Jahn-Teller distortion is present in $PrMnO_3$ at 150 K, while such distortion is not there in $CaMnO_3$.

(c) Spin wave density of states of $CaMnO_3$ and $PrMnO_3$

The magnetic transition for $CaMnO_3$ and $PrMnO_3$ are at about 130 K and 95 K respectively. As discussed in section IV(a) above, the excitations around 20 meV and 17 meV in $CaMnO_3$ and $PrMnO_3$ respectively are strong at low Q values, but at high Q values they are weaker, which indicates their predominate magnetic nature. However, we note that the separation of the phonon part ($\sim Q^2$) and the magnetic part (magnetic form factor squared) from the experimental data is difficult for strongly dispersed excitations and coherently scattering samples (which is the case for our samples as discussed in section IV(a) above). It should work for non-dispersed excitations, but not for dispersed. We have made an attempt to separate the magnetic and phonon contributions assuming a single-mode spin-wave excitation.

The variation of integrated intensity of the excitations for $CaMnO_3$ (energy range = 15-21 meV) and $PrMnO_3$ (energy range = 13-19 meV) as a function of Q for temperatures below the magnetic transition temperature is shown in Fig. 6. These excitations have contributions from both the phonon as well as magnetic excitations. The Mn atom is in Mn^{4+} and Mn^{3+} state in $CaMnO_3$ and $PrMnO_3$ respectively. The magnetic form factor for Mn^{3+} and Mn^{4+} are computed using the analytical relation [53] and shown (Fig. 6) as a continuous line. The Q-dependence of the dispersive magnetic modes has been compared with expectations for single mode spin wave excitations. It is clear that the fall of intensity at low Q values for both the compounds follow the magnetic form factor and confirm that the origin of the these excitations is magnetic in nature. At high Q values, the calculated form factor falls much below the experimental data, which indicates phonon contributions at high Q values.

McQueeney *et al* [38] has used the inelastic neutron scattering technique from polycrystalline samples to estimate the magnetic contribution on $LaMnO_3$, $LaVO_3$ and $LaFeO_3$. It has been shown that the magnetic scattering contribution can be obtained by subtracting the high Q data from low Q data by proper scaling factor. McQueeney *et al* [38] showed that the profile of the magnetic intensity could be

used to identify A- or G-type antiferromagnetic ordering. While the G-type ordering would lead to a sharp peak, the peak in case of the A-type ordering has a fall on the higher energy side that is less sharp than that in case of the G-type ordering and also has a hump on the higher energy side. We have analysed our inelastic neutron data using the same procedure. Figure 7 shows the S(Q, E) plots for the high Q and low Q as well as extracted magnetic intensity for $CaMnO_3$ and $PrMnO_3$ below their magnetic transition temperatures. It can be seen (Fig. 7) that the profile of the magnetic excitation for $CaMnO_3$ shows a peak centred around 20 meV with a sharp fall at higher energy side. The nature of the peak profile agrees very well with that of theoretical calculations of the spin-wave density of states for compounds exhibiting G-type antiferromagnetic ordering [38]. This is also in agreement with the experimental observations that $CaMnO_3$ below magnetic transition temperature (~130 K) undergoes a G type antiferromagnetic (AFM) transition [23].

$PrMnO_3$ is known to undergo A-type antiferromagnetic ordering [16]. As shown in Fig. 7, the magnetic profile for $PrMnO_3$ shows a peak centred around 16 meV with a fall on the higher energy side that is less sharp than that in case of $CaMnO_3$, which is consistent with the A-type ordering. We also observe a very weak peak at ~ 48 meV in $PrMnO_3$, which may probably arise from imperfect phonon subtraction.

(d) Magnetic ordering and calculated phonon spectra in the orthorhombic phase of $CaMnO_3$ and $PrMnO_3$

The theoretical calculations using LDA or GGA have limitations in "correlated" electrons systems [54]. For example, the band gap calculated by using these calculations is underestimated. These approximations (LDA/GGA) introduce a spurious Coulomb interaction of the electron with its own charge and introduce errors in localized states. However, the thermodynamical properties like phonon spectrum, specific heat and thermal expansion are found to be close enough with experiments [55]. We have seen in our previous studies using VASP Code on $GaFeO_3$ [55] that the inclusion of inner d/f electrons does not affect the phonon spectra and hence the thermodynamical properties. Our theoretical calculations were performed with taking into account of both the structure and magnetic interactions. For the title materials, it has been found that all the features of the phonon spectrum in the experimental data are fairly well reproduced by the calculations. Certain discrepancies between the calculated and measured phonon spectra arise due to the lack of an exact treatment of the exchange-correlation potential at the LDA/GGA level.

Another theoretical development to address the issue of strongly correlated system and improve the band gap is known as "hybrid functionals" method [56]. This functional uses a weighted mixture of

the exact exchange energy from the Hartree-Fock theory and the density-functional exchange. For phonon calculations, we have used supercell approach and the 2×2×2 supercell has 160 atoms. The phonon calculations of such a big system using this hybrid functional are computationally expensive, which makes the calculation of phonon properties of complex magnetic oxides very difficult.

In order to analyze the experimental neutron data, as stated above, first-principle calculations have been performed. The fully optimized structure of $CaMnO_3$ in both the "FRM" and "FRNM" configurations using both LDA and GGA exchange correlation functional are summarized in Table I. The calculated atomic positions are in good agreement with the experimental data. It can be seen that in both the LDA and GGA, the "FRM" calculated structures are found to close to the experimental data [57]. The LDA calculated lattice constants are found to be underestimated by 2% in comparison to the experimental data, while GGA gives slight overestimation of about 1%. As will be shown in Appendix, nonmagnetic structures are found to be dynamically unstable at T=0 K.

The comparison between the experimental data and the calculated phonon spectra from both the LDA and GGA are shown in Fig. 8. It can be seen that all the observed features in the experimental data are fairly well reproduced by the calculations. It is evident from this figure that below 55 meV, phonon calculation in fully relaxed magnetic configuration using LDA gives better agreement with the experimental data in comparison to GGA. However, for the spectral range above 55 meV, the calculated phonon spectrum using GGA describes the experiment better than LDA. The high energy (> 75 meV) phonons are due to Mn-O stretching modes. The observed discrepancy could be understood in terms of bond lengths. As shown in TABLE I, the LDA calculation underestimates the lattice parameters. The shorter bond lengths would shift the phonon spectra to higher energies in comparison to the experimental data. Similarly the slight overestimation of lattice parameter by GGA results in underestimation of the energies of the Mn-O modes in the calculation.

The phonon calculations (Fig. 9) for $PrMnO_3$ are carried out only in the fully relaxed magnetic configuration using GGA exchange correlation functions. All the observed features are fairly well reproduced (Fig. 9) by the computations. We note that the experimental structure and the measured neutron inelastic spectrum are found to be better described by the ab-initio calculations when the magnetic degrees of freedom are included in both the compounds, which highlight unambiguously a spin-phonon coupling character in $RMnO_3$. The atomistic contributions in the phonon spectra from the various calculations can be understood in terms of the partial density of states for $CaMnO_3$ and $PrMnO_3$. The details are given in Appendix.

We have also calculated the zone-centre phonon frequencies in the FRM structure of both the compounds with GGA. In the room temperature orthorhombic phase (*Pnma)* with 4 formulas per unit cell (20 atoms), the irreducible representations of the zone-centre optical phonons are

$$\Gamma_{optical} = (7A_g + 5B_{1g} + 7B_{2g} + 5B_{3g})_{Raman\text{-}active} + (9B_{1u} + 7B_{2u} + 9B_{3u})_{IR\text{-}active} + (8A_u)_{silent.}$$

Figure 10 compares our calculated zone-centre phonon frequencies with experimental and theoretical data available in the literature for both the compounds. Our calculations are found to be in fair agreement with reported data.

(e) High pressure phase stability of $CaMnO_3$ and $PrMnO_3$

Both $CaMnO_3$ and $PrMnO_3$ occur in the cubic phase at very high temperatures and undergo a sequence of phase transition with temperature and pressure. Our calculation of structural instabilities in the cubic phase and its relationship with phase transitions with temperature are given in Appendix. Pressure tunes the interplay between lattice and electronic degree of freedom to a much larger extent than any other parameter like temperature and magnetic field. In the present section, we discuss the effect of pressure on the structural distortions in the orthorhombic phase of $CaMnO_3$ and $PrMnO_3$. The main emphasis of this study is to investigate the pressure dependence of the likely Jahn-Teller distortion and existence of insulator to metal transition at high pressure. Recently, Mota *et al.* [13] reported a high pressure study of orthorhombic rare-earth manganites using a combination of synchrotron x ray diffraction and Raman scattering technique. The authors observed change in the diffraction patterns of $PrMnO_3$ and disappearance of the Raman spectrum with pressure. The authors [13] suspected that the change in the diffraction pattern might be related to a structural phase transition from orthorhombic to tetragonal (*I4/mcm*) structure at 45 GPa. On the other hand, the disappearance of Raman peak could also be due to insulator to metal transition. Hence the first principle simulation with pressure will help to overcome this ambiguity.

Figure 11 shows the calculated pressure dependence of the equivalent pseudo-cubic lattice parameters for the orthorhombic phase of (a) $CaMnO_3$ and (b) $PrMnO_3$ in FRM structures and using GGA, and comparison with experimental data reported in the literature [13, 59-60]. The computed (experimental) bulk modulus for $CaMnO_3$ and $PrMnO_3$ are found to be 185.4 (224 ± 25 [59]) GPa and 137.4 (139±4 [13]) GPa, respectively. It is evident from the figure that compression is more anisotropic

for $PrMnO_3$ as compared to $CaMnO_3$. The pressure dependence of the Jahn-Teller distortion, which is evidenced by the spatial distribution of Mn-O bond lengths (d) and defined as

$$\Delta = (\frac{1}{6})\sum_{n=1}^{6}\left[\frac{d_n - \langle d \rangle}{\langle d \rangle}\right]^2$$

along-with three Mn-O distances of the distorted MnO_6 octahedra, are shown in Figs. 11 (c) and (d). It is interesting to note that the computed Jahn-Teller distortion using the above relation is found to be two-orders lower for $CaMnO_3$ in comparison to that for $PrMnO_3$, and could be considered as zero. This result is satisfying as $CaMnO_3$ is known [14] to not possess any Jahn-Teller distortion.

The calculated variations of Mn-O distances with pressure are found to be highly anisotropic for $PrMnO_3$ but are isotropic for $CaMnO_3$. On increasing pressure on $PrMnO_3$, long Mn-O2 (l) distance decrease faster than the shorter Mn-O2(s) and Mn-O1, and becomes nearly equal at around 45 GPa. This nearly isotropic behavior of the Mn-O distance at high pressure is attributed to disappearance of Jahn-Teller distortion. Basically, application of external pressure opens the Mn-O-Mn angles and in turn shortens the Mn-O bond lengths, leading to less distorted octahedra. The calculated magnetic moment in the equilibrium structure at Mn site is 2.6 μ_B, which is in agreement with the experimental values of free Mn^{3+} (3.0). We found that at about 45 GPa, the Mn magnetic moment decreases to 1.0 μ_B which could be signature for insulator to metal transition.

Theoretically, we can predict the transition pressure in $PrMnO_3$ by comparing the enthalpy as a function of pressure for different phases. Figure 12 (a) depicts the computed pressure dependence of the difference in the enthalpy $\Delta H = H_{ortho} - H_{tetra}$ of orthorhombic and tetragonal phases. We find that the orthorhombic phase has the lowest enthalpy at low pressure below 19 GPa, as it is the well-known ground state of $PrMnO_3$ at T=0 K. However, at pressure above 19 GPa, the tetragonal phase becomes favorable over the orthorhombic phase. The value of the pressure is in agreement with the pressure where shear strain becomes unstable (see Fig. 7 of Ref.13). Mota *el al.* [13] reported that the strain analysis does not give any evidence for the suppression of the Jahn-Teller distortion at this pressure. If we recall Fig. 11 (d), we find that the computed Jahn-Teller distortion decreases rapidly up to this pressure and then it decreases slowly. Based on combined diffraction and Raman data, Mota *el al.* [13] suspected that $PrMnO_3$ may undergo orthorhombic to tetragonal structural phase transition at around 45 GPa. As mentioned above, the calculated pressure dependence of the enthalpy suggests that the tetragonal phase is energetically favorable over the orthorhombic phase above P= 19 GPa. In order to investigate the dynamical stability of tetragonal phase, we computed the phonon dispersion relation (Fig. 12 (b)) in the entire Brillouin zone at 30 GPa. The presence of unstable phonon modes in the tetragonal phase clearly suggests that although the tetragonal phase is energetically favored over

orthorhombic phase, it is dynamically unstable. Therefore, the calculations do not support the possibility of orthorhombic to tetragonal phase transition in $PrMnO_3$ around 45 GPa.

As shown in Figure 11, the suppression of the Jahn-Teller distortion occurs at 45 GPa. Further we find that the magnetic moment at Mn site is also quenched at the same pressure. The suppression of the Jahn-Teller distortion is expected to decrease the volume at high pressures. Thus change in the volume of the unit cell in the experimental data at around 45 GPa may be associated with disappearance of Jahn-Teller distortion followed by insulator to metal transition. Our band structure calculation also suggests that $PrMO_3$ becomes poor metal above 45 GPa. Similar observation is also reported in case of $LaMnO_3$ [61], which shows the suppression of the Jahn-Teller distortion and insulator to metal transition by application of pressure. In $LaMnO_3$, the Jahn-Teller distortion and orbital ordering are known to be completely suppressed well below the insulator to metal transition. In contrast to $LaMnO_3$, in the present case, we notice that the suppression of Jahn-Teller distortion and insulator to metal transition occur simultaneously.

V. CONCLUSIONS

We have reported inelastic neutron scattering measurements of the $CaMnO_3$ and $PrMnO_3$ in a wide temperature range up to 1251 K. The excitations at 20 meV and 17 meV are found to be associated with the magnetic origin for $CaMnO_3$ and $PrMnO_3$ respectively. The neutron inelastic spectra also show changes across the magnetic as well as structural phase transitions temperatures in both the compounds. Measurements show that in spite of similar structure the presence of Jahn-Teller distortion $PrMnO_3$ might results in broad peaks in the phonon spectra in comparison to $CaMnO_3$ where it exhibits well-defined peaks. The ab-initio phonon calculations are found to be in fair agreement with the experimental phonon spectra if magnetic interactions are included.

We also discussed the effect of pressure on the structural distortions in the orthorhombic phase of $CaMnO_3$ and $PrMnO_3$. On application of pressure, the variations of Mn-O distances are isotropic for $CaMnO_3$ and highly anisotropic for $PrMnO_3$. Theoretical calculation for $PrMnO_3$ suggests that suppression of Jahn-Teller distortion and insulator to metal transition occur simultaneously, which is in-contrast to the behavior in $LaMnO_3$. We also find that at high pressure above 19 GPa, although the tetragonal phase in $PrMnO_3$ is energetically favored over the orthorhombic phase, it is dynamically unstable.

Acknowledgements

The neutron scattering experiments at Oak Ridge National Laboratory's Spallation Neutron Source were sponsored by the Scientific User Facilities Division, Office of Basic Energy Sciences, U. S. Department of Energy. S. L. Chaplot would like to thank the Department of Atomic Energy, India for the award of Raja Ramanna Fellowship.

1. S. Jin, T. H. Tiefel, M. McCormack, R. A. Fastnacht, R. Ramesh, and L. H. Chen, Science **264**, 413 (1994). G. C. Milward, M. J. Calderon, and P. B. Littlewood, *Nature* **433**, 607 (2005).

2. D. Preziosi, M. Alexe, D. Hesse, and M. Salluzzo, Phys. Rev. Lett. **115**, 157401 (2015).

3. Y. F. Nie, P. D. C. King, C. H. Kim, M. Uchida, H. I. Wei, B. D. Faeth, J. P. Ruf, J. P. C. Ruff, L. Xie, X. Pan, C. J. Fennie, D. G. Schlom, and K. M. Shen, Phys. Rev. Lett. **114**, 016401 (2015).

4. C. Ulrich, G. Khaliullin, M. Guennou, H. Roth, T. Lorenz, and B. Keimer, Phys. Rev. Lett. **115**, 156403 (2015).

5. L. L. Lev, J. Krempaský, U. Staub, V. A. Rogalev, T. Schmitt, M. Shi, P. Blaha, A. S. Mishchenko, A. A. Veligzhanin, Y. V. Zubavichus, M. B. Tsetlin, H. Volfová, J. Braun, J. Minár, and V. N. Strocov, Phys. Rev. Lett. **114**, 237601 (2015).

6. L. Chaix, S. de Brion, S. Petit, R. Ballou, L.-P. Regnault, J. Ollivier, J.-B. Brubach, P. Roy, J. Debray, P. Lejay, A. Cano, E. Ressouche, and V. Simonet, Phys. Rev. Lett. **112**, 137201 (2014).

7. N. Ganguli and P. J. Kelly, Phys. Rev. Lett. **113**, 127201 (2014).

8. Yue Jia, R.V. Chopdekar, E. Arenholz, A. T. Young, M. A. Marcus, A. Mehta, and Y. Takamura, Phys. Rev B **92**, 094407 (2015).

9. M. Hoffmann, V. S. Borisov, S. Ostanin, I. Mertig, W. Hergert, and A. Ernst, Phys. Rev B **92**, 094427 (2015); A. Furrer, A. Podlesnyak, and K. W. Kramer, Phys. Rev B **92**, 104415 (2015).

10. Y. W. Windsor, S. W. Huang, Y. Hu, L. Rettig, A. Alberca, K. Shimamoto, V. Scagnoli, T. Lippert, C. W. Schneider, and U. Staub, Phys. Rev. Lett. **113**, 167202 (2014).

11. P. Barone, D. Di Sante, and S. Picozzi, Phys. Rev B **89**, 144104 (2014).

12. J. Hong, A. Stroppa, J. Íñiguez, S. Picozzi, and D. Vanderbilt, Phys. Rev B **85**, 054417 (2012)

13. D. A. Mota, A. Almeida, V. H. Rodrigues, M. M. R. Costa, P. Tavares, P. Bouvier, M. Guennou, J. Kreisel, and J. Agostinho Moreira, Phys. Rev B **90**, 054104 (2014).

14. S. Bhattacharjee, E. Bousquet, and Philippe Ghosez, Physical Rev. Lett. **102**, 117602 (2009).

15. U. Aschauer, R. Pfenninger, S. M. Selbach, T. Grande, and N. A. Spaldin, Phys. Rev B **88**, 054111 (2013); N. Hamdad, B.Bouhafs, Physica B **405**, 4595 (2010).

16. J. Hemberger, M. Brando, R. Wehn, V. Yu. Ivanov, A. A. Mukhin, A. M. Balbashov, and A. Loidl, Phys. Rev B **69**, 064418 (2004).

17. L. Bocher, M. H. Aguirre, R. Robert, D. Logvinovich, S. Bakardjieva, J. Hejtmanek, and A. Weidenkaff, Acta Mater. **57**, 5667 (2009).

18. K. R. Poeppelmeier, and M. E. Leonowicz, J. C. Scanlon, J. Solid State Chem. **45**, 71 (1982).

19. D. Sousa, M. R. Nunes, C. Silveira, I. Matos, A. B. Lopes, and M. E. M. Jorge, Mater. Chem. Phys. **109**, 311 (2008).

20. X. J. Fan, H. Koinuma, and T. Hasegawa, Physica B **329–333,** 723 (2003).

21. N. Kumar, H. Kishan, A. Rao, and V. P. S. Awana, J. Alloys Compd. **502** 283 (2010).

22. Y. Wang, Y. Sui, P. Ren, L. Wang, X. Wang, W. Su and H. Fan, Inorg. Chem. **49** 3216 (2010).

23. M. Nicastro and C. H. Patterson *Phys. Rev.* B **65** 205111 (2002). C. R. Wiebe and J. E. Greedan, J. S. Gardner, Z. Zeng and M. Greenblatt, Phys. Rev B **64**, 064421 (2001).

24. H. Taguchi, M. Nagao, T. Sato, and M. Shimada, J. of Solid Stat. Chem. **78**, 312, (1989).

25. R. Kajimoto, H. Mochizuki and H. Yoshizawa, S. Okamoto†, S. Ishihara, Phys. Rev B **69**, 054433 (2004); H. Yoshizawa, H. Kawano, Y. Tomioka, and Y. Tokura, Phys. Rev. B **52** R13 145 (1995).

26. Z. Jirak, S. Krupicˇka, Z. Simsa, M. Dlouha and S. Vratislav, J.Magn.Magn.Mater.**53** 153 (1985); Y. Tomioka, A. Asamitsu, H. Kuwahara, Y. Moritomo, and Y. Tokura, Phys. Rev. B **53**, R1689 (1996).

27. C. Martin, A. Maignan, M. Hervieu, and B. Raveau Phys. Rev. B **60,** 12191 (1999); M. V. Zimmermann, C. S. Nelson, J. P. Hill, D. Gibbs, M. Blume, D. Casa, B. Keimer, Y. Murakami, C.-C. Kao, C. Venkataraman, T. Gog, Y. Tomioka, and Y. Tokura, Phys. Rev. B **64,** 195133 (2001).

28. I. Anisimov, I. S. Elfimov, and M. A. Korotin, K. Terakura, Phys. Rev. B **55**, 15494 (1997).

29. J. Hong, A. Stroppa, J.´Iˇniguez, S. Picozzi, and D. Vanderbilt, Phys. Rev. B **85**, 054417 (2012).

30. M. Molinari, D. A. Tompsett, S. C. Parker, F. Azoughb, and R. Freerb, J. Mater. Chem. A **2**, 14109 (2014); E. S. Bozin, A. Sartbaeva, H. Zheng , S. A. Wells, J. F. Mitchell, Th. Proffen, M. F. Thorpe, and S. J. L. Billinge, J. of Phys. and Chem. of Solids **69**, 2146 (2008).

31. R. Kajimoto, H. Mochizuki, H. Yoshizawa, H. Shintani, T. Kimura, and Y. Tokupra, J. of the Phys. Soc. of Japan **74**, 2430 (2005); B. Dabrowskia, S. Kolesnika, A. Baszczukb, O. Chmaissema, T. Maxwella, and J. Maisa, Journal of Solid State Chemistry **178**, 629 (2005).

32. M. N. Iliev, M. V. Abrashev, J. Laverdière, S. Jandl, M. M. Gospodinov, Y.-Q. Wang, and Y.-Y. Sun, Phys. Rev B **73**, 064302 (2006); H. C. Gupta and U. Tripathi, PMC Physics B, 1:9 (2008).

33. S. Bhattacharjee, E. Bousquet and P. Ghosez; J. Phys.: Condens. Matter **20,** 255229, (2008).

34. F. P. Zhang, Q. M. Lu, X. Zhang and J. X. Zhang, Journal of Alloys and Compounds **509**, 542 (2011).

35. H. Tsukahara, S. Ishibashi, and K. Terakura, Phys. Rev B **81**, 214108 (2010).

36. B. Bouadjemi, S. Bentata, A. Abbad, W. Benstaali, and B. Bouhafs, Solid State Comm. **168**, 6 (2013).

37. J. A. Fernandez-Baca, P. Dai, H. Y. Hwang, C. Kloc, and S- W. Cheong, Phys. Rev Lett. 80, 4012 (1998); H. Y. Hwang, P. Dai, S W. Cheong, G. Aeppli, D. A. Tennant, and H. A. Mook, Phys. Rev Lett. **80**, 1316 (1998); P. Dai, H. Y. Hwang, J. Zhang, J. A. Ferndez-Baca, S. W. Cheong, C. Kloc, Y. Tomioka and Y. Tokura Phys. Rev B **61**, 9553 (2000); P. Dai, J. A. Ferndez-Baca, E. W. Plummer, Y. Tomioka and Y. Tokura Phys. Rev B **64**, 224429 (2001); Y. Chen, B. G. Ueland, J. W. Lynn, G. L. Bychkov, S. N. Barilo and Y. M. Mukovskii Phys. Rev B **78**, 212301 (2008); S. E. Hahn, A. A. Podlesnyak, G. Ehlers, G. E. Granroth, R. S. Fishman, A. I. Kolesnikov, E. Pomjakushina and K. Conder, Phys. Rev B **89** 014420 (2014).

38. R. J. McQueeney, J Q Yan, S Chang and J. Ma, Phys. Rev B **78**, 184417 (2008).

39. G. E. Granroth, D. H. Vandergriff, and S. E. Nagler, Phys. B: Condens. Matter **385–86**, 1104 (2006).

40. G. E. Granroth, A. I. Kolesnikov, T. E. Sherline, J. P. Clancy, K. A. Ross, J. P. C. Ruff, B. D. Gaulin, and S. E. Nagler, J. Phys.: Conf. Ser. **251**, 012058 (2010).

41. D. L. Price, Neutron scattering, Academic Press, Orlando, 1986; J. M. Carpenter and D. L. Price, Phys. Rev. Lett. **54**, 441 (1985).

42. O. Arnold, J. C. Bilheux, J. M. Borreguero, A. Buts, S. I. Campbell, L. Chapon, M. Doucet, N. Draper, R. Ferraz Leal, M. A. Gigg, V. E. Lynch, A. Markvardsen, D. J. Mikkelson, R. L. Mikkelson, R. Miller, K. Palmen, P. Parker, G. Passos, T. G. Perring, P. F. Peterson, S. Ren, M. A. Reuter, A. T. Savici, J. W. Taylor, R. J. Taylor, R. Tolchenov, W. Zhou, and J. Zikovsky, Mantid - Data analysis and visualization package for neutron scattering and μSR experiments. *Nuclear Instr. Meth. Phys. Res. Section A*: **764**, 156-166 (2014).

43. R. Azuah, L. Kneller, Y. Qiu, P. Tregenna-Piggott, C. Brown, J. Copley, and R. Dimeo, J. Res. Natl. Inst. Stan. Technol. **114**, 341 (2009).

44. G. Kresse and D. Joubert, Phys. Rev. B **59**, 1758 (1999).

45. A. Dal Corso, Phys. Rev. B **82**, 075116 (2010).

46. P. Hohenberg and W. Kohn, Phys. Rev. **136**, B864 (1964).

47. W. Kohn and L. J. Sham, Phys. Rev. **140**, A1133 (1965).

48. G. Kresse and J. Furthmüller, Computational Materials Science **6**, 15 (1996).

49. J. P. Perdew, K. Burke and M. Ernzerhof, Phys. Rev. Lett. **77**, 3865 (1996).

50. J. P. Perdew and A. Zunger, Phys. Rev. B **23**, 5048 (1981).

51. H. J. Monkhorst and J. D. Pack, Phys. Rev. B **13**, 5188 (1976).

52. Phonon software, K. Parlinksi, 2003.

53. A. J. Dianoux and G. Lander, Neutron Data Booklet (OCP Science, Philadelphia, 2003).

54. J. Hong, A. Stroppa, J. Íñiguez, S. Picozzi, and D. Vanderbilt, Phys. Rev. B **85**, 054417 (2012).

55. M. K. Gupta, R. Mittal, M. Zbiri, R. Singh, S. Rols, H. Schober and S. L. Chaplot Phys. Rev. B. **90**, 134304 (2014).

56. J. Heyd, G. E. Scuseria, and M. Ernzerhof, J. Chem. Phys. 118, 8207 (2003); J. Heyd, G. E. Scuseria, and M. Ernzerhof, J. Chem. Phys. **124**, 219906 (2006).

57. M. V. Abrashev, J. Backstrom, L. Borjesson, V. N. Popov, R. A. Chakalov, N. Kolev, R.-L. Meng, and M. N. Iliev, Phys. Rev. B **65**, 184301, (2002).

58. R. Sopracase, G. Gruener, E. Olive, and J. C. Soret, Physica B **405**, 45 (2010); I. Fedorov, J. Lorenzana , P. Dore, G. De Marzi, P. Maselli, P. Calvani, S. W. Cheong, S. Koval, and R. Migoni, Phys. Rev. B **60**, 11875 (1999).

59. L. Ying-Xin, Q. Shan, J. Jian-Zhong, K. Takumi and S. Guang-Hai, Chinese Physics C **34**, 1025 (2010); W. Paszkowicz, S. M. Woodley, P. Piszora, B. Bojanowski, J. Pi¸etosa, Y. Cerenius, S. Carlson, and C. Martin, Appl. Phys. A **112**, 839 (2013); J. Pietosa, W. Paszkowicz, R. Minikayev, J. Nowak; C. Lathe, and C. Martin, Powder Diffraction **26**, 262 (2011).

60. D. Sánchez, J. A. Alonso and M. J. Martínez-Lope, J. Chem. Soc., Dalton Trans. 4422 (2002).

61. I. Loa, P. Adler, A. Grzechnik, K. Syassen, U. Schwarz, M. Hanfland, G. Kh. Rozenberg, P. Gorodetsky,4 and M. P. Pasternak, Phys. Rev Lett. **87**, 125501 (2001).

62. W. Cochran, Adv. Phys. **9**, 387 (1960).

TABLE I. Comparison of experimental and theoretical structural parameters in the antiferromagnetic orthorhombic phase (space group: *Pnma)* of $CaMnO_3$. The Wyckoff sites of the atoms are given in the brackets. "FRM", "FRNM" and "PNM" refer to fully relaxed magnetic, fully relaxed non-magnetic and partially relaxed non magnetic calculations, respectively.

Structural Parameters	Expt. [18]	Ref. [33]	**This work**					
			GGA			LDA		
			FRM	PNM	FRNM	FRM	PNM	FRNM
A_o (Å)	5.279	5.287	5.3380	5.3380	5.3148	5.2011	5.2011	5.189
B_o (Å)	7.448	7.498	7.4977	7.4977	7.4238	7.2933	7.2933	7.2386
C_o (Å)	5.264	5.235	5.2949	5.2949	5.2645	5.1396	5.1396	5.1084
Ca (4c)								
x	0.035	0.040	0.040	0.038	0.038	0.045	0.044	0.045
y	0.250	0.250	0.250	0.250	0.250	0.250	0.250	0.250
z	-0.009	-0.008	-0.008	-0.007	-0.007	-0.009	-0.008	-0.009
Mn (4b)								
x	0.00	0.00	0.00	0.00	0.00	0.00	0.00	0.00
y	0.00	0.00	0.00	0.00	0.00	0.00	0.00	0.00
z	0.500	0.500	0.500	0.500	0.500	0.500	0.500	0.500
O1 (4c)								
x	0.493	0.485	0.489	0.483	0.483	0.488	0.491	0.491
y	0.250	0.250	0.250	0.250	0.250	0.250	0.250	0.250
z	0.068	0.071	0.068	0.062	0.062	0.073	0.070	0.070
O2 (8d)								
x	0.290	0.287	0.288	0.287	0.287	0.290	0.290	0.290
y	0.030	0.036	0.035	0.032	0.033	0.031	0.036	0.037
z	-0.289	-0.288	-0.289	-0.288	-0.288	-0.289	-0.289	-0.289

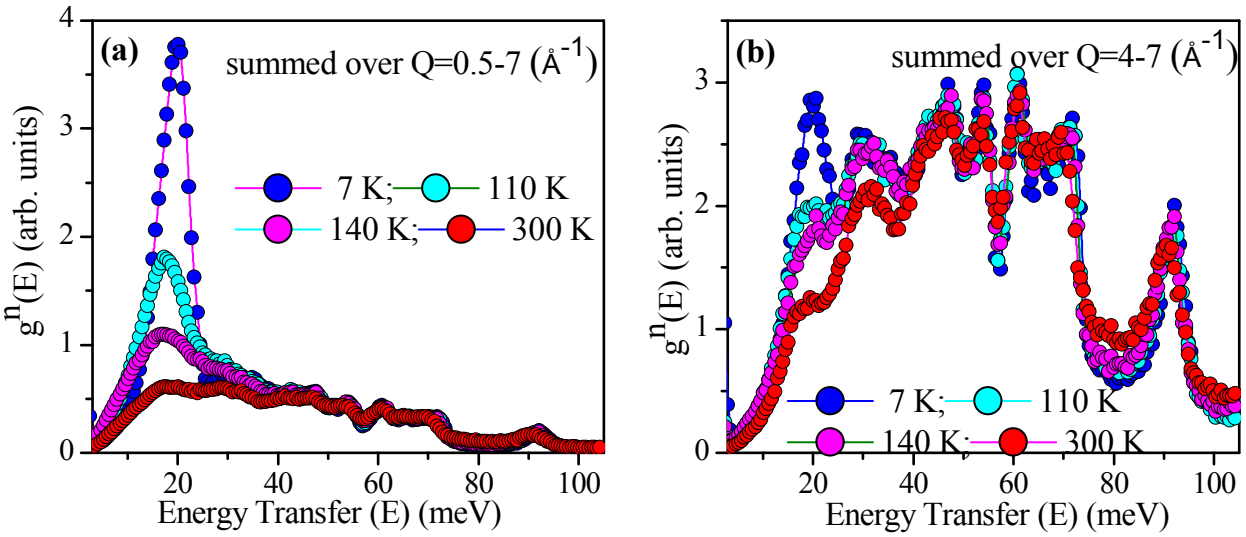

FIG 1. (Color online) The neutron inelastic spectra of $CaMnO_3$ at low temperatures, the data were summed over (a) Q=0.5-7 Å^{-1} and (b) Q=4-7 Å^{-1} respectively. The peak at ~20 meV is due to spin-wave excitations, not due to phonons (1 meV=8.0585 cm^{-1}).

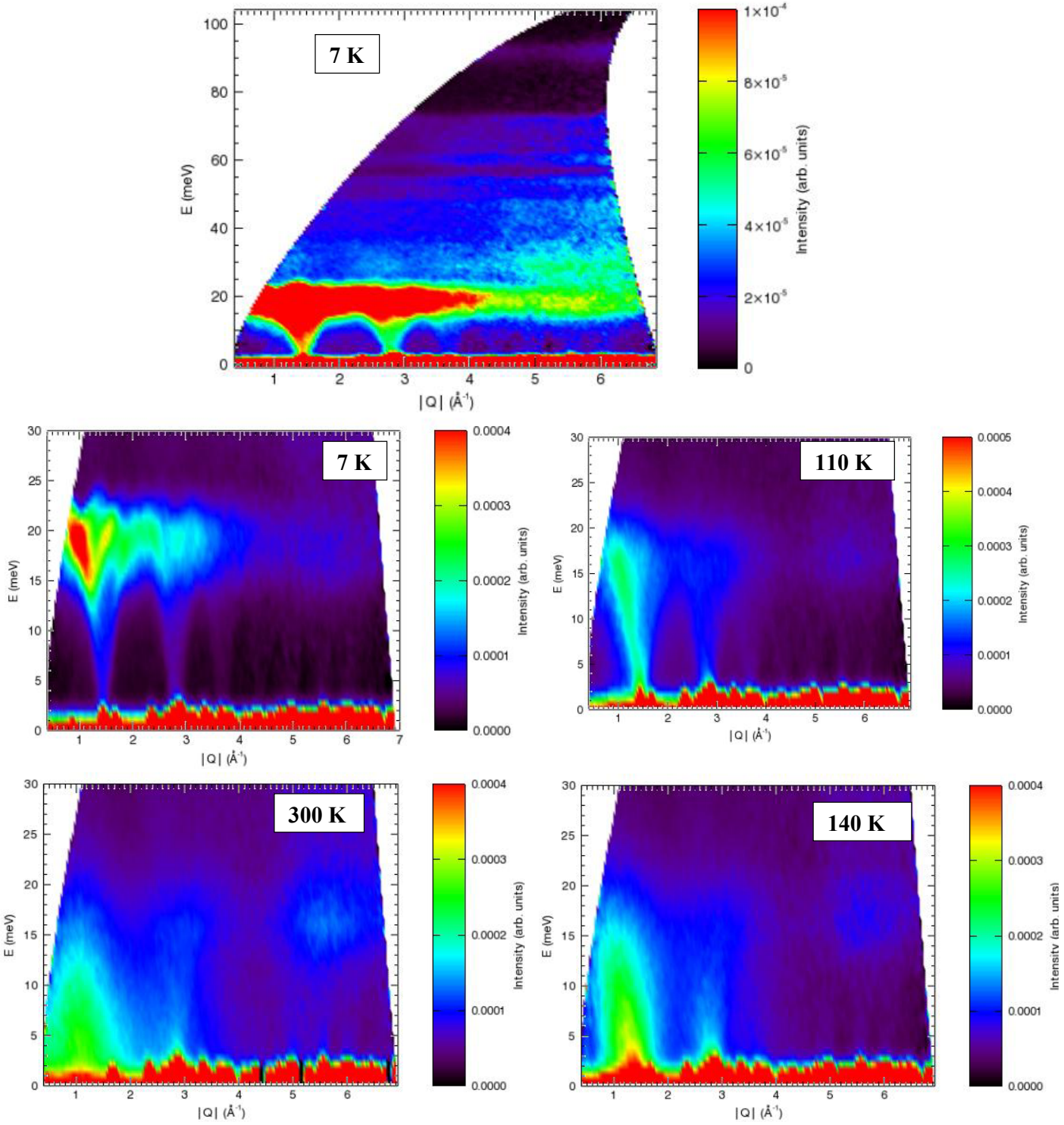

FIG 2. (Color online) The (Q,E) contour plot of S(Q,E) data for $CaMnO_3$ at T=7 K measured at SEQUOIA with incident neutron energy of 110 meV is shown at top. Strong intensity excitations at low temperatures (7 K and 110 K) below E=20 meV and Q=3.5 $Å^{-1}$ are due to magnetic spin-wave excitations. The excitations around 30, 45, 55, 60, 65, 70, and 90 meV are due to phonons (their intensities increase with increasing Q).

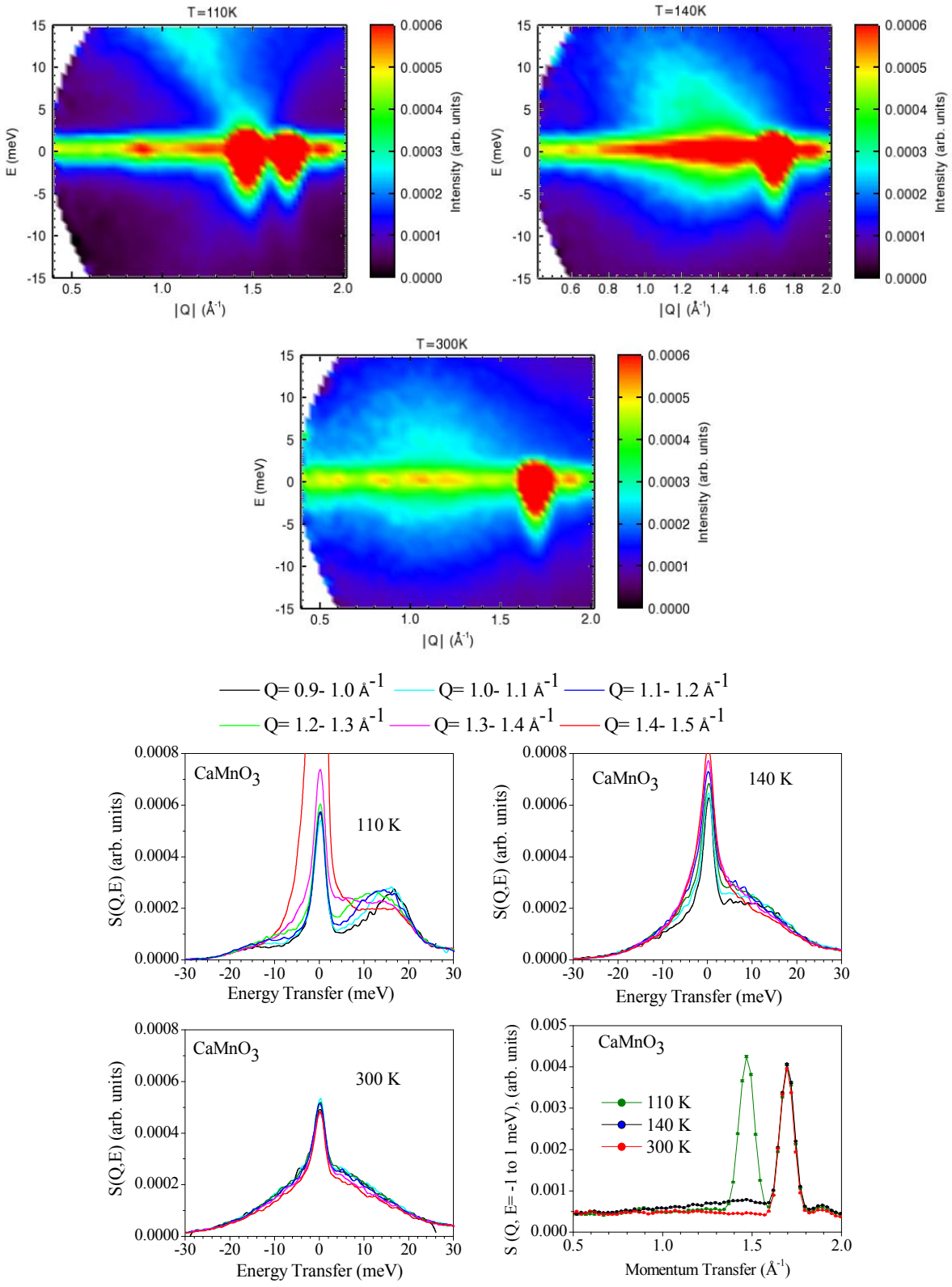

FIG 3. (Color online) Top panel: The (Q,E) contour plot of S(Q,E) spectra for $CaMnO_3$ Bottom panel: Temperature dependent neutron inelastic spectra of $CaMnO_3$ summed over various Q-range. Bottom Right panel: Temperature dependent neutron elastic spectra S(Q) of $CaMnO_3$.

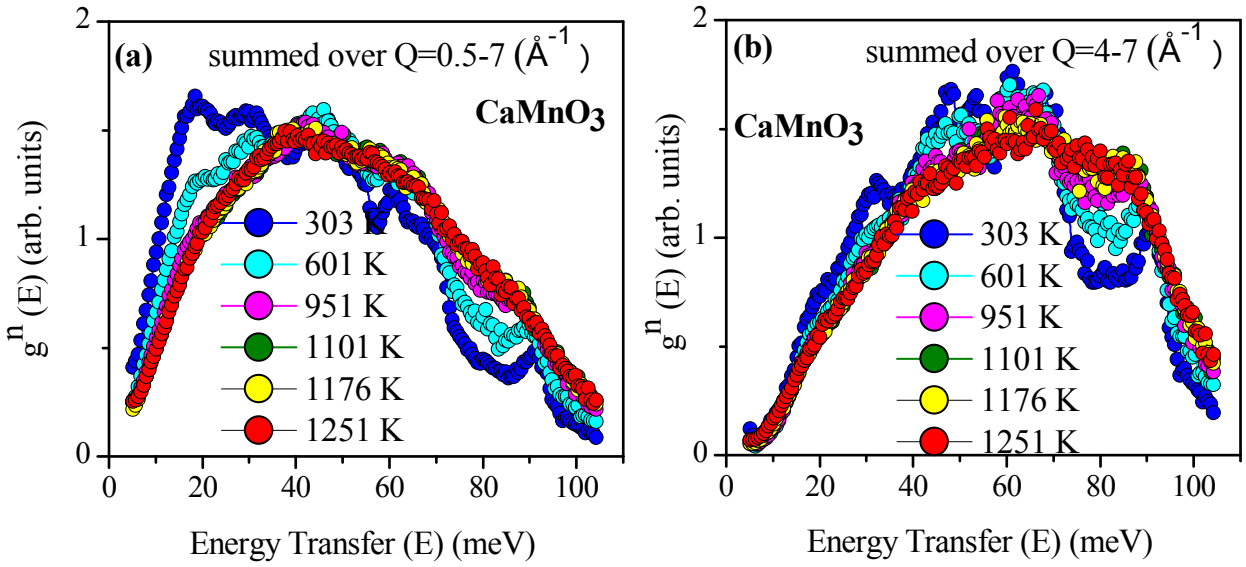

FIG 4. (Color online) The temperature dependence (above 300 K) of the neutron inelastic spectra of $CaMnO_3$, the data were summed over (a) Q=0.5-7 A^{-1} and (b) Q=4-7 A^{-1} respectively.

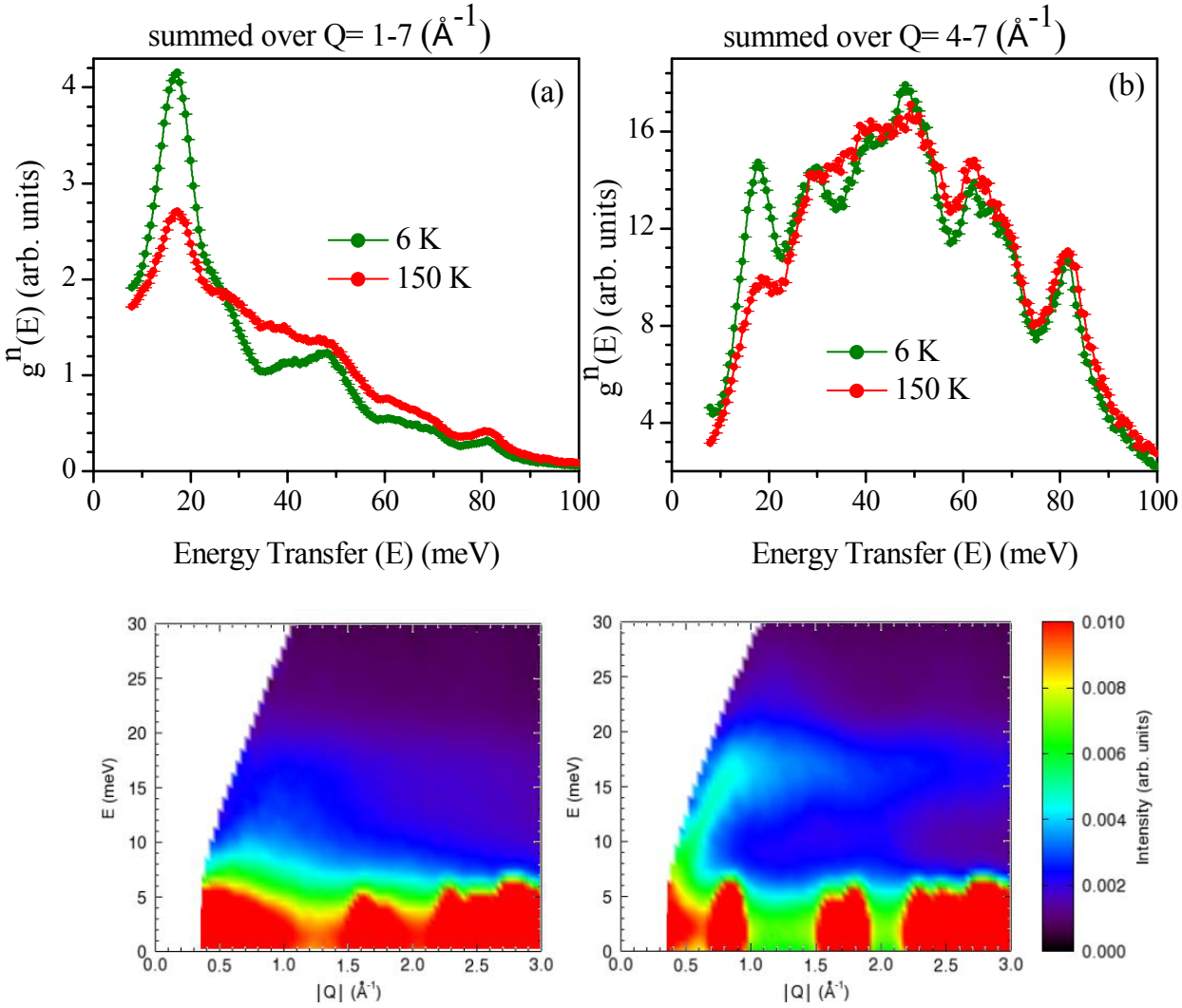

FIG 5. (Color online) Top panel: Temperature dependent neutron inelastic spectra of $PrMnO_3$ summed over various Q-range. Bottom panel: Contour plot of S(Q,E) spectra for $PrMnO_3$ measured at 6 K (right) and 150 K (left). A dispersed spin wave excitation is clearly seen below 20 meV and 1.5 A^{-1} at 6 K. In 150 K spectra, weakly dispersed magnetic excitation around 15 meV is observed.

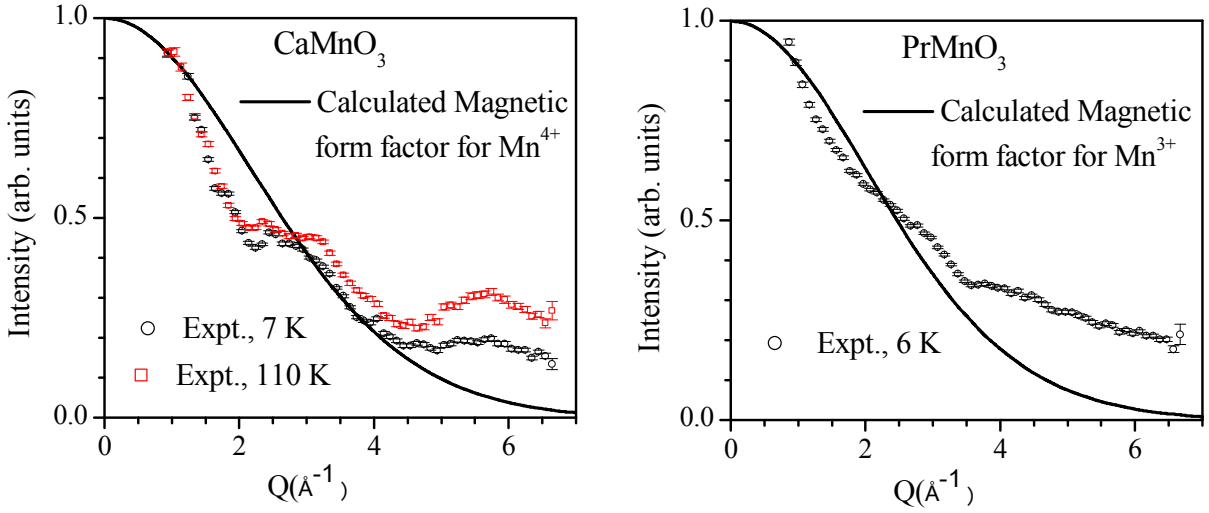

FIG 6. (Color online) The variation of integrated intensity of the excitation for $CaMnO_3$ (energy range = 15-21 meV) (left side panel) and $PrMnO_3$ (energy range = 13-19 meV) (right side panel) at different temperature. The magnetic form factor for Mn^{3+} and Mn^{4+} are computed using the analytical relation and shown as a continuous line. To compare the energy dependence of the dispersive magnetic modes with expectations for single mode spin wave excitations, intensity of dispersive magnetic modes is scaling by a constant factor.

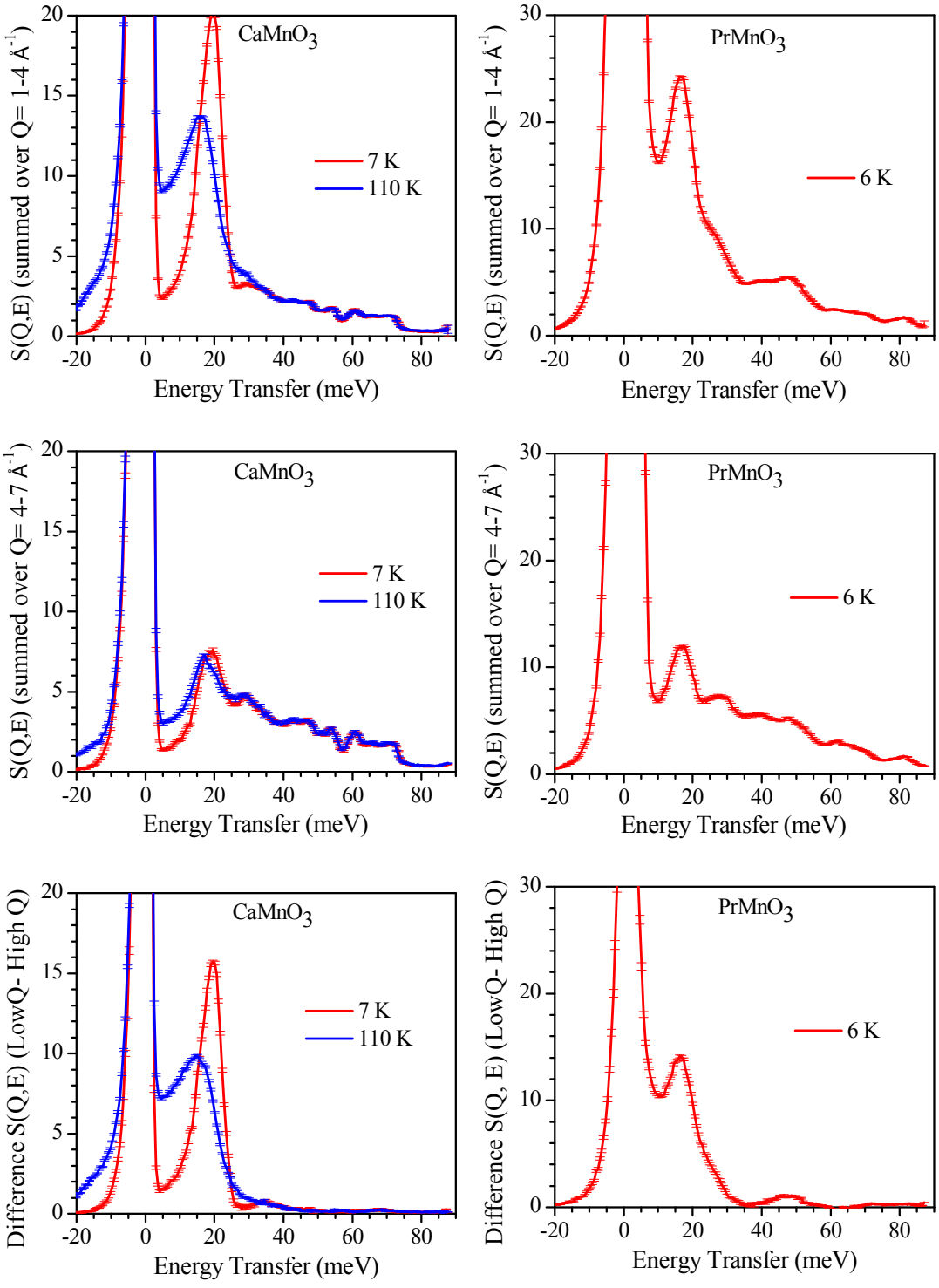

FIG 7. (Color online) Extracted Magnetic contributions (intensity difference between low Q and high Q) in neutron inelastic spectra of $CaMnO_3$ and $PrMnO_3$ at temperatures below T_N from polycrystalline samples.

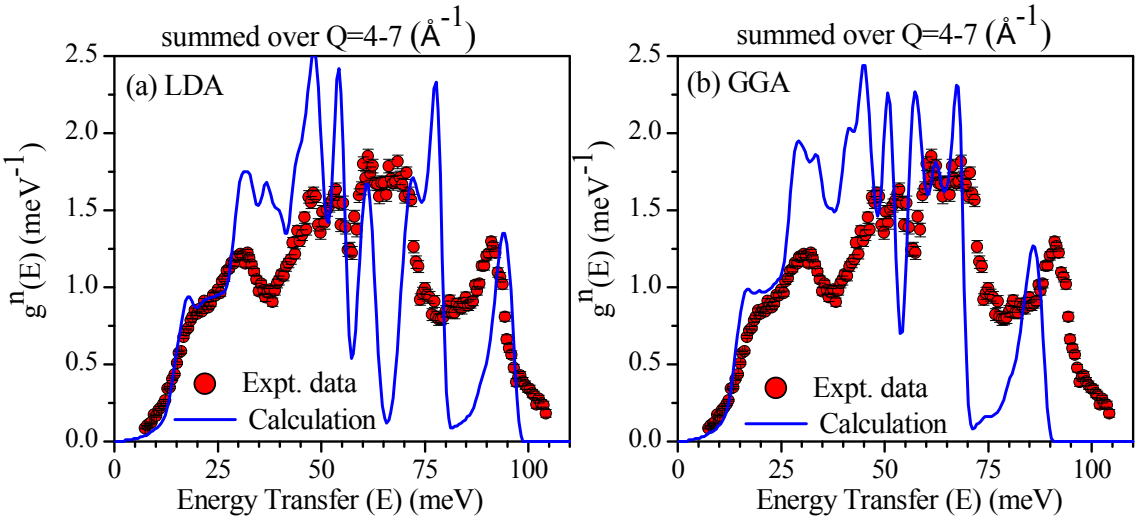

FIG 8. (Color online) Comparison between the experimental (T=300 K) and calculated neutron inelastic spectra of $CaMnO_3$ using (a) local density approximation and (b) generalized gradient approximation. Experimental data are summed over 4-7 Å^{-1}. The phonon calculations are carried out in the fully relaxed magnetic (FM) configuration. The calculated phonon spectra have been convoluted with a Gaussian of FWHM of 4.5 meV to account for the effect of energy resolution in the experiment.

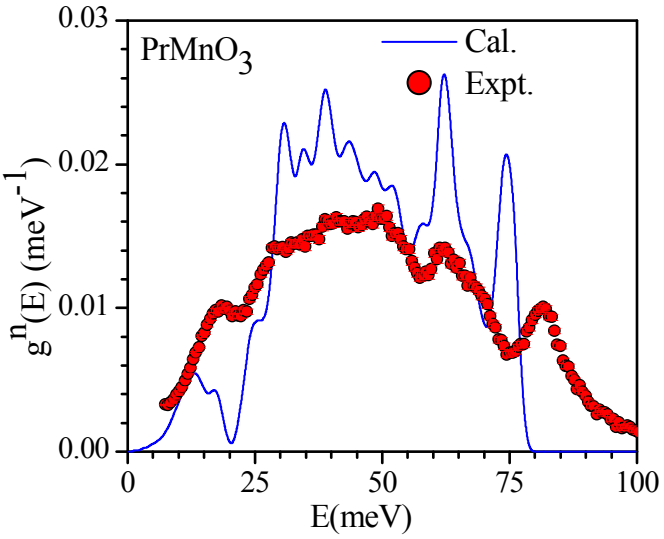

FIG 9. (Color online) Comparison between the experimental (T= 150 K) and calculated phonon spectra in $PrMnO_3$. Experimental data are summed over 4-7 Å^{-1}. The phonon calculations are carried out in the fully relaxed magnetic (FRM) configuration in the generalized gradient approximation (GGA).

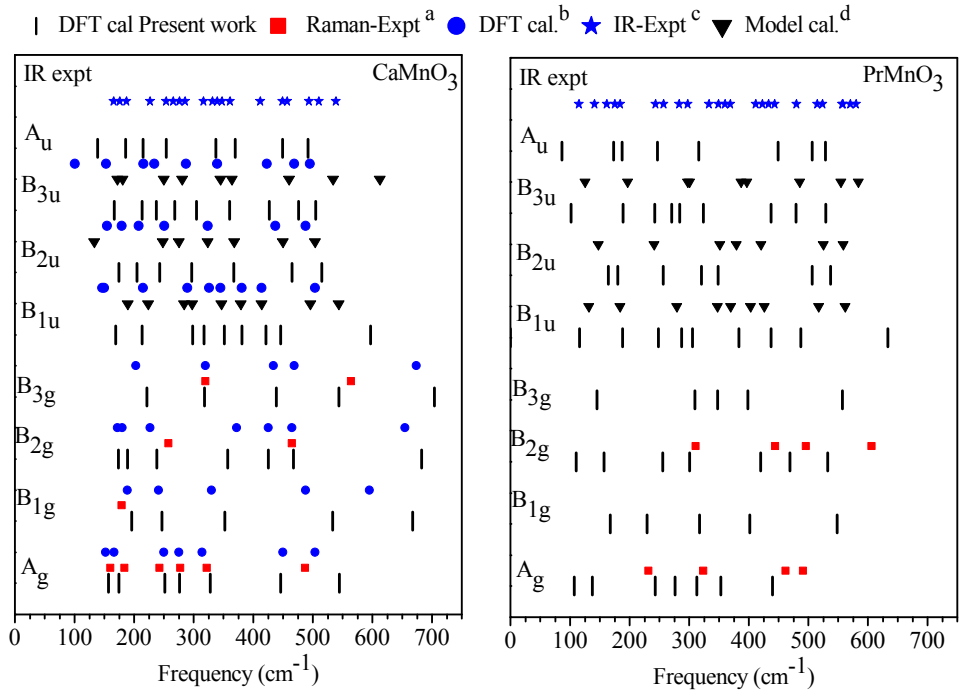

FIG 10. (Color online) Comparison of the calculated long-wavelength phonon frequencies (in FRM structures and using GGA) with the available data in literature. The references for reported experimental and calculated optical long-wavelength data are as [a] Raman experimental data (ref. 57 for $CaMnO_3$; ref. 32 for $PrMnO_3$), [b] first principle DFT calculation (ref. 33 for $CaMnO_3$), [c] IR experimental data (ref. 58 for $CaMnO_3$ and $PrMnO_3$) and (d) lattice dynamical calculation using potential model (ref. 58 for $CaMnO_3$; ref. 32 for $PrMnO_3$).

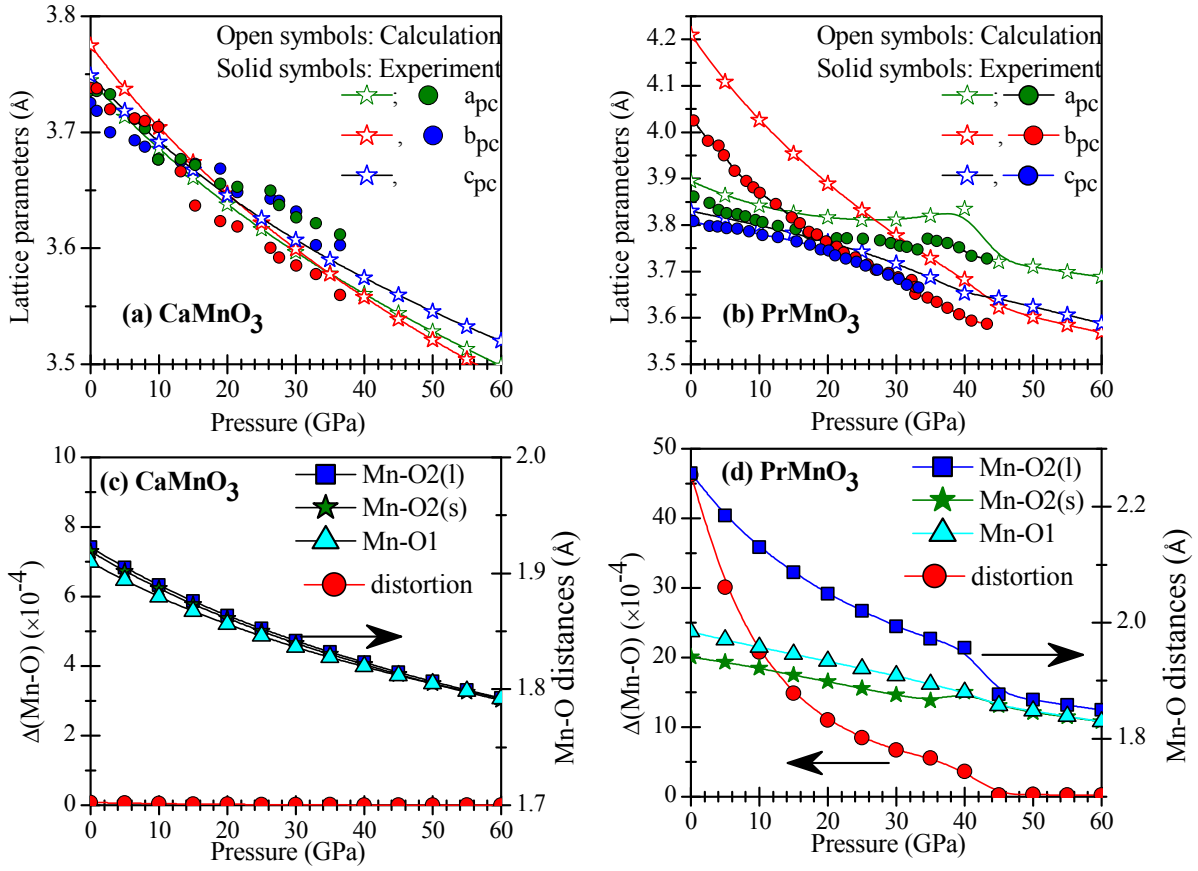

FIG **11.** (Color online) Pressure dependence of the calculated pseudocubic lattice parameters (in FRM structures and using GGA) for (a) $CaMnO_3$ and (b) $PrMnO_3$ compared to reported experimental data for $CaMnO_3$ [59] and $PrMnO_3$ [13] respectively. Pressure dependence of Mn-O bond length and distortion of MnO_6 ochtahedra as calculated are shown in (c) $CaMnO_3$ and (d) $PrMnO_3$, respectively.

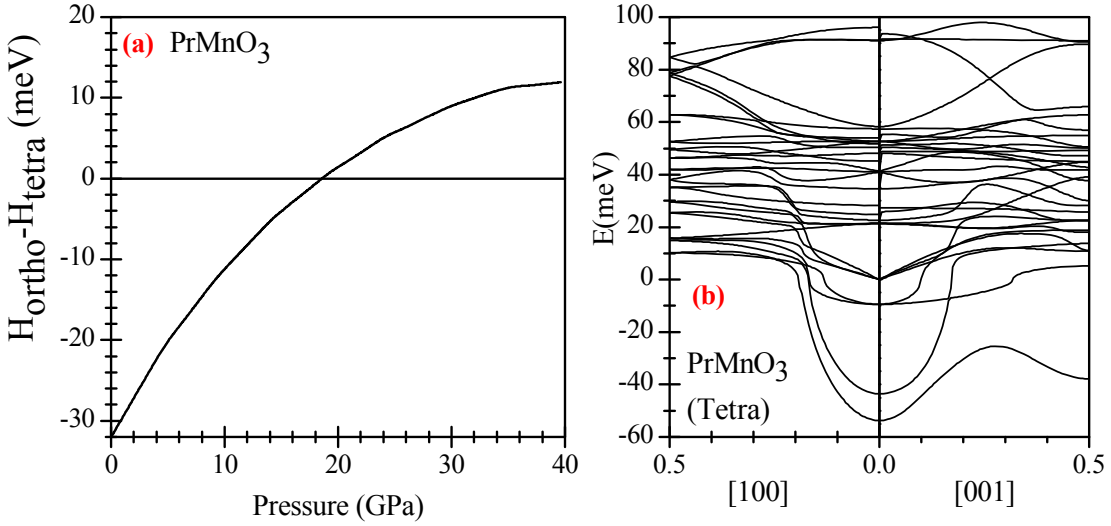

FIG 12**.** (a) Enthalpy difference (ΔH) between the orthorhombic (*Pnma*) and tetragonal (*I4/mcm*) phases of $PrMnO_3$ as calculated using ab-inito DFT calculation (in FRM structures and using GGA). The computed phonon dispersion relations for $PrMnO_3$ in tetragonal phase at P= 30 GPa is shown in (b).

Appendix

A: Partial Phonon Density of State for $CaMnO_3$ and $PrMnO_3$

The contributions in the phonon spectrum from specific atoms can be understood in terms of the partial density of states. The computed atomistic partial phonon density of states in orthorhombic $CaMnO_3$ show (Fig. A. 1 (a)) that the contribution of the oxygen atoms spreads over the whole energy range, while the Mn atoms contribute mainly up to 75 meV. The contribution due to Ca atoms extends up to 50 meV. Above 75 meV, the dynamics is mainly due to the Mn-O stretching modes. It can be seen (Fig. A.1 (a)) that the contributions of Ca and Mn are nearly the same in the calculations performed using LDA and GGA, while there are significant differences in the partial contribution from the O atoms. The difference in the calculated partial contribution is mainly in the stretching modes region which is very sensitive to the unit cell volume. The underestimation or overestimation of energy of modes is related to the calculated structures as given in TABLE I. Results of the FRM-GGA calculations are found to be close to the experimental data. Consequently in the following we adopt the GGA density functional.

To study the effect of magnetic interactions, the phonon spectra were calculated in three different configurations as explained in Sec. III ("FRM", "FRNM", and "PNM") and shown in Figure A. 1 (b). It is evident from this figure that the phonon spectra calculated using PNM as well as FRNM result in unstable modes. Thus, it is evident that magnetic interactions as incorporated in FRM are very important for obtaining the dynamically stable structure.

The computed atomistic partial density of states of various atoms in orthorhombic $PrMnO_3$ shows (Fig. A. 2) that the contribution of the Mn and oxygen atoms spreads over the whole energy range up to 75 meV, while the contribution due to Pr atoms extends up to 50 meV. It should be noted that in the present case contributions due to the Mn-O stretching modes do not extend above 75 meV, while in $CaMnO_3$ the energy range of these modes is up to 90 meV. The comparison between the calculated and experimental phonon spectra shows that stretching modes are underestimated (Fig. A. 2) in the phonon calculations. The calculations of zone centre phonon modes, as shown in Fig. 8, also confirm the same.

B: Structural instabilities in the cubic phase of $CaMnO_3$ and $PrMnO_3$ and phase transition to the tetragonal phase at high temperature

The cubic phase in both $CaMnO_3$ and $PrMnO_3$ occurs at very high temperatures. It is expected to be dynamically unstable at low temperature and stabilized by anharmonicity at high temperature. It is important to identify the unstable modes in order to understand the phase transition mechanism. In order to obtain the equilibrium lattice parameter for the cubic phase of $CaMnO_3$ and $PrMnO_3$, we performed structural optimization by minimizing the total energy with respect to structural parameters. The cubic phase of $CaMnO_3$ and $PrMnO_3$ are known to be G- type antiferromagnetic and ferromagnetic respectively. The calculations have been performed by including the magnetic ordering. The relaxed lattice parameters for $CaMnO_3$ and $PrMnO_3$ are found to be a= 3.7588 Å and a= 3.8920 Å, respectively. Figure B.1 shows the computed phonon dispersion relation using GGA. It is evident from this figure that phonon dispersions in the two compounds show noticeable differences especially at high energies. The phonons contribute up to 110 meV for $CaMnO_3$ and up to 80 meV for $PrMnO_3$, respectively. This difference could be understood in terms of difference in bond lengths for these compounds. The lattice parameter of cubic $CaMnO_3$ is smaller than that of $PrMnO_3$ and hence shorter bond lengths would shift the phonon energies to higher side.

Careful inspection of phonon dispersion relation reveals the presence of polar instability (zone centre phonon instabilities) with an imaginary frequency $\omega_{FE} \approx 20i$ meV for $CaMnO_3$ and $\omega_{FE} \approx 8i$ meV in $PrMnO_3$ respectively. We also observe antiferrodistortive (AFD) instability (zone boundary phonon instabilities) at R and M points in the Brilloun zone for both the compounds. Condensation of these AFD instabilities results in phase transition from cubic to the tetragonal and then to the orthorhombic phase. It is also remarkable to notice that as we move from R to M point, the strength of instability is quite similar for $CaMnO_3$ ($\omega_{AFD} \approx 30i$ meV at R and M points), however, it becomes larger for $PrMnO_3$ ($\omega_{AFD} \approx 30i$ meV at R point and $\omega_{AFD} \approx 24i$ meV at M point). Interestingly, the branches along the Γ-X, X-M, Γ-R, and Γ-M directions, show dramatic changes when reaching the X, R and M points. When moving away from R to M, two unstable modes are detected. One of them is rather flat and the other one shows rapid stiffening and becomes stable. Moreover, moving across the Γ-X, the unstable modes become stable at X point for $CaMnO_3$ and it does not show appreciable change for $PrMnO_3$. For $CaMnO_3$, Bhattacharjee et al [14] also observed both (polar and AFD) types of instability. They reported that the polar instability is very sensitive to volume and it is suppressed by anharmonic effects once the dominant antiferrodistortive (AFD) instability is condensed.

Now, we would like to comment on the mechanism of the cubic *(Pm-3m)* to tetragonal *(I4/mcm)* phase transition that occurs in $CaMnO_3$ and Pr MnO_3 at high temperature. This phase transition is known [62] to be driven by R point phonon instability. To identify the specific phonon, we have calculated the phonon energies in the high temperature cubic phase with a super cell of $\sqrt{2}\times\sqrt{2}\times2$, which is equivalent to the unit cell of the tetragonal phase (*I4/mcm*). The structure parameters used in phonon calculations are given in Table II. The distortion vector has been obtained with respect to ideal cubic phase. The calculated eigen vector of the unstable R point mode in the super cell ($\sqrt{2}\times\sqrt{2}\times2$) of cubic phase is also given in Table B. I. It is evident from the Table that only O2 atoms displace from its ideal positions. The eigen vector of the R point mode is in good agreement with the distortion vector. The displacement pattern of the unstable mode at the R point in the cubic phase is shown in Fig. B.2, which indicates anti phase rotation of in plane oxygens in the two layers containing MnO_6.

TABLE B. I. The calculated structures of $CaMnO_3$ in the tetragonal (*I4/mcm*) and super cell (√2×√2×2) of cubic phase. The super cell (√2×√2×2) of cubic phase is equivalent to the tetragonal (I4/mcm) phase. The unit cell in the *I4/mcm* space group has O1, O2, Ca and Mn atoms at the 4a(0 0 0.25), 8h (x y 0), 4b (0.5 0 0.25) and 4c(0 0 0) Wyckoff sites respectively. The distortion vector is obtained from the difference in atomic coordinates of the tetragonal phase (I4/mcm) and super cell cubic phase. The eigen vector of the unstable R point mode in the super cell (√2×√2×2) of cubic phase (Pm-3m) is also given. The amplitude of the eigen vector of O2 is scaled to match with the distortion vector.

Atom		**Super cell (√2×√2×2) of cubic phase (*Pm-3m*)**	**Tetragonal phase (*I4/mcm*)**	**Distortion vector in fractional coordinates**	**Eigen vector of the unstable R point mode in the super cell of cubic phase**
	a_t (Å) c_t (Å)	5.315 (Å) 7.518(Å)	5.279 7.621		
O1	*x* *y* *z*	0.00 0.00 0.25	0.00 0.00 0.25	0.00 0.00 0.00	0.00 0.00 0.00
O2	*x* *y* *z*	0.25 0.25 0.00	0.31 0.19 0.00	0.06 -0.06 0.00	0.06 -0.06 0.00
Ca	*x* *y* *z*	0.50 0.00 0.25	0.50 0.00 0.25	0.00 0.00 0.00	0.00 0.00 0.00
Mn	*x* *y* *z*	0.00 0.00 0.00	0.00 0.00 0.00	0.00 0.00 0.00	0.00 0.00 0.00

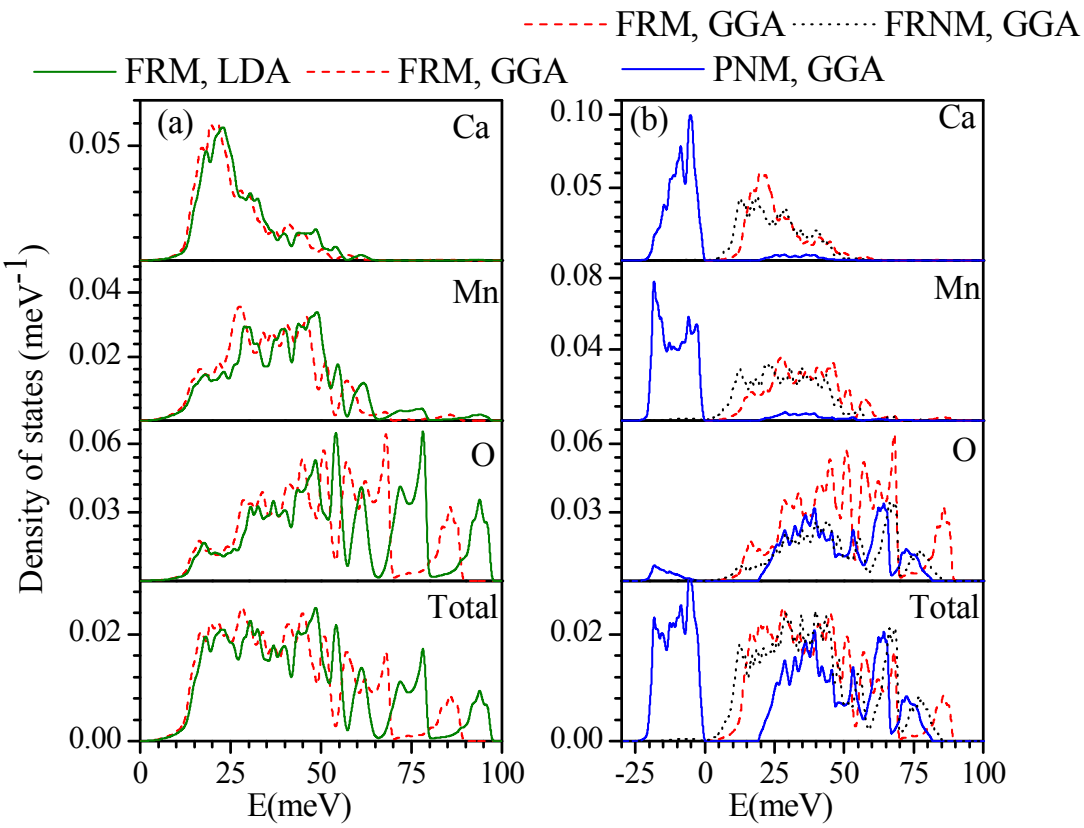

FIG A. 1. (Color online) (a) The calculated partial phonon density of states of various atoms in $CaMnO_3$ with in LDA and GGA approximations. (b) The calculated partial density of states of $CaMnO_3$ in various configurations with in GGA. "FRM", "FNM" and "PNM" refer to fully relaxed magnetic, fully relaxed non-magnetic and partially relaxed non magnetic calculations, respectively. The energies of unstable modes in PNM-GGA are plotted as negative energies.

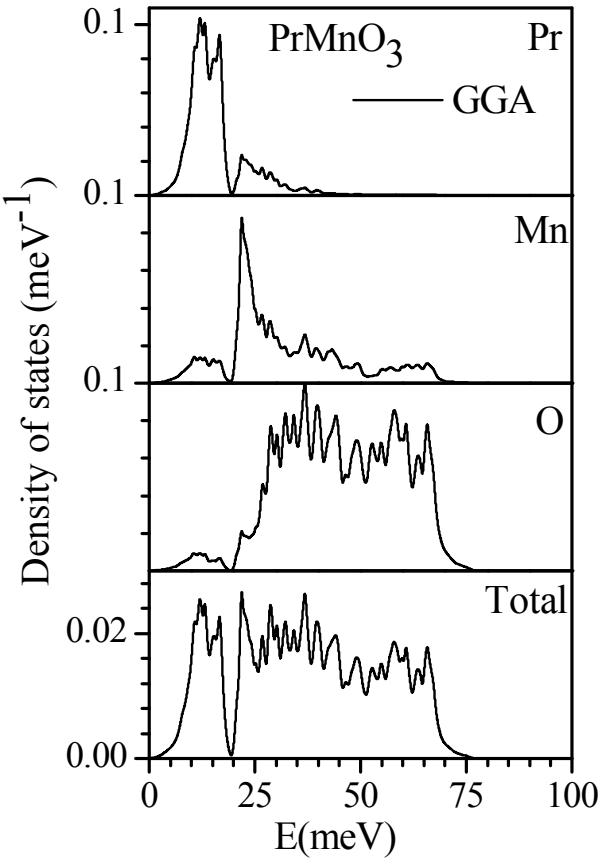

FIG A. 2. (Color online) The calculated partial phonon density of states of various atoms in $PrMnO_3$. The phonon calculations are carried out in the fully relaxed magnetic (FRM) configuration in the generalized gradient approximation (GGA).

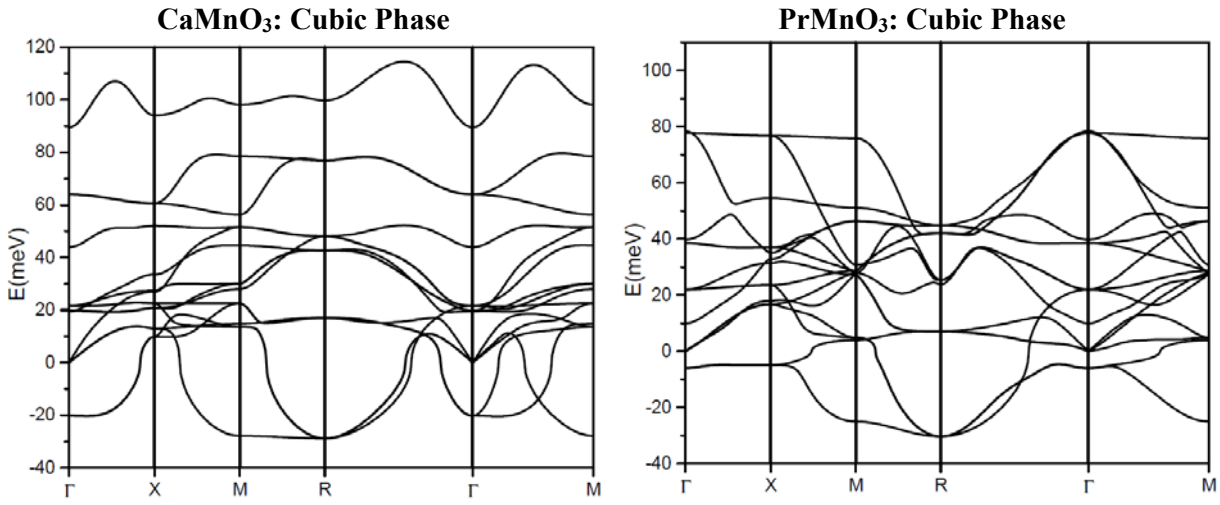

FIG **B. 1.** Computed phonon dispersion relations for $CaMnO_3$ (left panel) and $PrMnO_3$ (right panel) using generalized gradient approximation (GGA) in cubic phase.

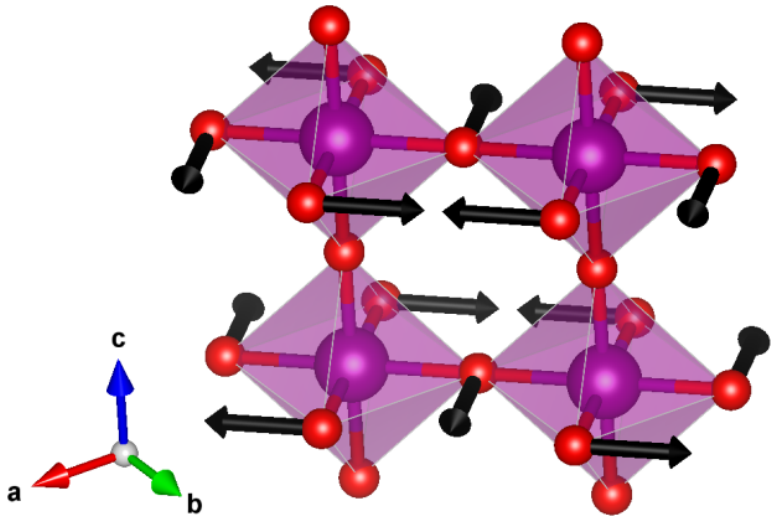

FIG B. 2**.** (Color online) The displacements pattern of unstable mode at the R point in the cubic phase.